Investigating flow patterns and related dynamics in multi-instability turbulent plasmas using a three-point cross-phase time delay estimation velocimetry scheme

C. Brandt[1,2], S. C. Thakur[1,3], G. R. Tynan[1,3]
Center for Energy Research, University of California–San Diego, La Jolla, California 92093-0417, USA
Max-Planck-Institute for Plasma Physics, Wendelsteinstr. 1, D-17491 Greifswald, Germany and
Center for Momentum Transport and Flow Organization, La Jolla, California 92093-0417, USA

Complexities of flow patterns in the azimuthal cross-section of a cylindrical magnetized helicon plasma and the corresponding plasma dynamics are investigated by means of a novel scheme for time delay estimation velocimetry. The advantage of this introduced method is the capability of calculating the time-averaged 2D velocity fields of propagating wave-like structures and patterns in complex spatiotemporal data. It is able to distinguish and visualize details of simultaneously present superimposed entangled dynamics and it can be applied to fluid-like systems exhibiting frequently repeating patterns (e.g., waves in plasmas, waves in fluids, dynamics in planetary atmospheres, etc.). The velocity calculations are based on time delay estimation obtained from cross-phase analysis of time series. Each velocity vector is unambiguously calculated from three time series measured at different spatial points. This method, when applied to fast imaging, has been crucial to understand the rich plasma dynamics in the azimuthal cross-section of a cylindrical linear magnetized helicon plasma. The capabilities and the limitations of this velocimetry method are discussed and demonstrated for two completely different plasma regimes, i.e., for quasi-coherent wave dynamics and for complex broadband wave dynamics involving simultaneously present multiple instabilities.

PACS numbers: 52.35.Ra, 52.35.-g, 52.25.Xz, 52.35.Kt, 52.35.Mw, 47.80.Cb

1. INTRODUCTION

Inherent energy sources in plasmas such as density gradients and ion and electron temperature gradients give rise to various instabilities leading to the formation of flows and waves which can nonlinearly interact and drive the system to dynamics dominated by turbulence [1]. Inverse cascades of energy via vortex mergers or vortex interactions with a weak non-zero background flow can lead to large scale flows in the system [2, 3]. Moreover the existence of a radial electric field in plasmas can also give rise to flows. On the other hand, flows themselves can be sources driving other kinds of instabilities. The most common flow related instability is the Kelvin-Helmholtz instability that arises due to sheared flows [4, 5]. In this regard, to understand several different phenomena in a plasma, the accurate measurement of the plasma flows is crucial. It gives important insight to understand both the origin of the flows and their effects on the complex plasma dynamics. For example, a recent study in the Controlled Shear Decorrelation eXperiment (CSDX) has shown coexisting multiple plasma instabilities located at spatially separated regions [6]. Depending on the plasma parameters (e.g., magnetic field and input power), various regimes develop, each characterized by different dynamics. For example for increasing magnetic fields the plasma evolves from a purely density gradient driven collisional drift wave (CDW) mode dominated regime to a system of weak turbulence where the CDW modes are superimposed on a broad background of plasma density fluctuations driven by other instabilities. Other studies also show transitions between various instabilities depending on external operation parameters and boundary conditions [7, 8]. In such systems, understanding the flows and the spatiotemporal patterns gives physical insight to the phenomena being studied. However, getting proper measurements of the flows and wave velocities has not been trivial, as the system, being very rich in complexity, shows several phenomena occurring at different temporal and spatial scales.

Typically there are two approaches to determine velocities from spatiotemporal data: (i) pattern matching algorithms and (ii) cross correlation techniques. In fluids, the instantaneous flow velocity field can be measured by imaging seeded tracer particles assuming negligible inertia. This method is only valid when the introduction of the foreign particles does not perturb the original flows being studied. The velocity field is then represented by the trajectories of the tracers and it can be estimated by particle tracking velocimetry (PTV) or particle image velocimetry (PIV). These methods have been successfully applied to study the flow fields in fluids and gases (e.g., the atmosphere) [9–12]. In PTV, pattern matching algorithms are applied to calculate the distance that a recognizable structure moves between consecutive measurements. PIV methods calculate the velocity by local spatial cross-correlation between interrogation windows of sequential images. For example, in dusty plasmas the dynamics of dust particles can be investigated within the plasma background by applying conventional PIV methods [13] to reconstruct single trajectories [14] using the dust as the tracer particles. But in general, tracer particles can not be used to measure the very complex fast flows and associated wave dynamics in a plasma. Structures that are born are typically obliged to change in shape, size and amplitude due to wave-wave and wave-particle electrodynamic interactions and eventually clear away. In some cases propagating waves, pat-

terns or structures of density formations can themselves serve as "tracer objects" in a loose sense (as these "tracers" change the shape and size with time and space). In Refs. [15–19] a cross-correlation velocimetry method is used to track blob structures in the separatrix regions of tokamak experiments (e.g., Alcator C-Mod, ASDEX Upgrade). Even if the blobs change its size and shape, this method is reported to be robust and tracks the structures resulting in a realistic velocity field of propagating blobs. Other PTV methods are also capable of measuring the instantaneous velocity field of propagating wave-like structures in a plasma [20, 21]. Ref. [22] is a detailed study of optical flow and pattern matching techniques introducing a hybrid approach between cross-correlation and pattern matching. However, all these PIV and PTV methods are less suited to investigate broadband turbulence dynamics, where a superposition of different instabilities and related spatial structures following different velocity fields is present. Here the dynamics can be very entangled and events at various timescales can occur at the same place, and vice versa at various spatial scales at the same time.

In case of frequently repeating wave-like events – the requirement of a measurable peak in the frequency domain of interest – time delay estimation (TDE) cross-correlation techniques can be useful to determine averaged frequency-resolved velocities [23–28]. Such methods are typically applied to time series measured at two spatially separated points. By assuming that the structures are propagating from one point to the other, in the particular direction of a line joining the two points, the velocity vector in this direction is calculated. However, this procedure leads to erroneous results when the velocity vector of the propagating structures is not along the straight line joining the two points as used for the standard two-point TDE method [22, 29]. Effectively the measurement of the velocity between two points can accurately give only one dimensional velocity. When the two-point TDE method is extended to study velocities in two dimensions, there are inherent systematic errors, that are not necessarily taken into account during routine use of this method. This discrepancy is shown in Fig. 1 of Ref. [29]. For example, we take a look at a simple case of motion in two dimensions in the radial-azimuthal plane. For a circular-shaped blob having a pure azimuthal motion, two point TDE will give the correct azimuthal velocity if the two points are chosen spatially separated in the azimuthal direction at the same radial position. However, for the same system, if the two points of interrogation are chosen to be spatially separated in the radial direction at the same azimuthal angle, the estimated velocity would be infinite. Points chosen other than in line with the azimuthal motion thus lead to artificially enhanced velocity estimates. Moreover, for tilted structures, any efforts to estimate the radial and azimuthal velocity from two radially separated points using two point TDE would give large errors. This can lead to serious concerns in the use of two-point TDE to estimate two dimensional velocity vectors using an array of points, as in standard gas puff imaging or beam emission spectroscopy [18]. To avoid these kind of discrepancies, we propose using three spatially separated points and show that in this method, these errors can be reduced.

This letter reports a method for the calculation of the time-averaged 2D velocity field $\mathbf{v}(x, y) = v_x\mathbf{e}_x + v_y\mathbf{e}_y$ of wave-like structures and patterns propagating in a two-dimensional plane. Using the assumption of propagating plane waves this work concentrates on the dynamics of wave structures. Each single velocity vector is frequency-selectively calculated from time series measured at three spatially separated points aligned in a triangular geometry in the plane. The velocity vectors are calculated by 3-point cross-phase time delay estimation (in the following called 3-point CP-TDE). From the cross-power spectral density (CPSD) the cross-phase is used to calculate the (time averaged) time delay that structures need to propagate between the pairs of points. Since the cross-phase depends on the frequency, the chosen frequency interval for averaging the velocity vector field is a very crucial parameter. Due to the self-consistent solution of two velocity vector components measured by the three points, this velocimetry method cannot result in infinite velocity values. The method should be applicable to space-time data measured with any kind of spatiotemporal diagnostic in plasma physics (plasma probe array, visible light imaging, imaging techniques like gas puff imaging, beam emission spectroscopy, X-ray imaging, etc.) and in fluids in general.

Figure 1 illustrates the capability of the 3-point CP-TDE velocimetry introduced in this work compared to usual 2-point TDE velocimetry. In the case when lo-

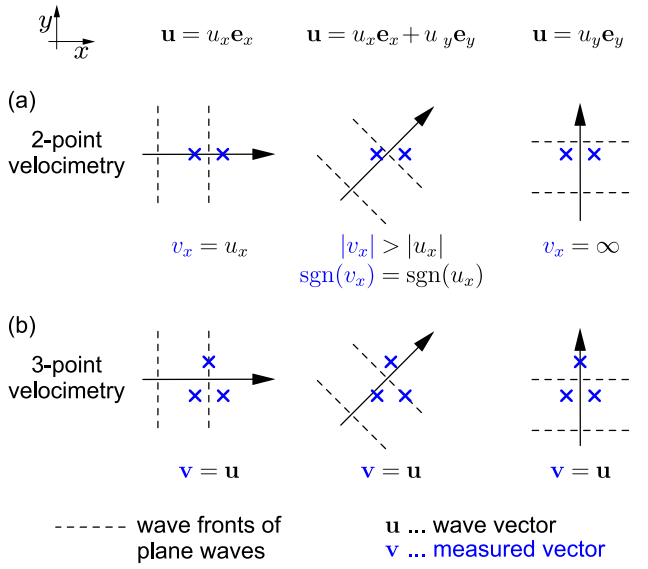

FIG. 1: (Color online) Capability of (a) 2-point TDE velocimetry and (b) 3-point CP-TDE velocimetry. For three different wave vectors $\mathbf{u}$ the relations to the measured vector $\mathbf{v}$ are illustrated. Plane wave fronts are assumed.

cally plane waves can be assumed, the 3-point CP-TDE velocimetry can measure the time-averaged 2D velocity field, i.e., the measured average velocity vectors $\mathbf{v}$ equal the average wave vectors $\mathbf{u}$. Globally the wave fronts are allowed to change their directions, but in scales smaller than the wavelength the plane wave assumption is needed. The method has limitations when applied to obtain the average velocity field of single structures, such as blobs or eddies, especially when their structures are tilted. But the method also works for these cases when the shape of the structures is random or when the location of their occurence is random. In Sec. 2 this issue is discussed in more details. In plasmas one distinguishes between different types of velocities, ranging from the plasma flow velocity, a zoo of plasma waves and their velocities and the velocity of certain plasma structures (e.g., eddies and blobs). Propagating structures in plasmas can be measured by spatiotemporal diagnostics like Langmuir probe arrays or fast imaging. In this letter, we apply the described 3-point CP-TDE technique to space-time visible light measurements of the dynamics in a cylindrical helicon plasma. It is assumed that the structures observed as propagating waves or patterns of light emission are linked to density [21, 30, 31].

This paper is organized as follows. In Sec. 2 the 3-point CP-TDE velocimetry method is introduced. Section 3 starts with the description of the experimental setup and diagnostics of CSDX and introduces two different plasma regimes in the helicon discharge mode used for applying the introduced velocimetry method. Section 4 shows the results of velocimetry studied in the different plasma regimes. The results are discussed in Sec. 5 and summarized in Sec. 6.

2. 3-POINT CROSS-PHASE TIME DELAY ESTIMATION VELOCIMETRY

The method of extracting the average 2D velocity field is applicable to spatiotemporal data of fluid-like systems when the dynamics exhibits a non-random average quasi-periodic component resulting in a peak in the frequency domain. This can be waves or structures propagating along a temporary stable trajectory, e.g., cloud motion in the atmosphere, rotating structures and waves in a plasma or vortex motion in the atmosphere. A high enough spatial and temporal resolution of the data is desirable to resolve the spatial distances and the directions of the structures propagating between consecutive measurements. At least the spatial and temporal Nyquist limits need to be fulfilled, i.e., $d < \lambda_{\min}/2$ and $f_{\text{sample}} > 2f_{\text{wave,max}}$ with d being the spatial distance between the points, $\lambda_{\min}$ the shortest detectable wavelength, f_{sample} the sampling frequency and $f_{\text{wave,max}}$ the maximal detectable frequency. In this work the average 2D velocity field of propagating structures and waves in a helicon plasma is calculated from spatiotemporal data of fast camera measurements.

Figure 2 illustrates the geometry and the parameters used for the 3-point CP-TDE method. To determine the average velocity vector $\mathbf{v}(x_i, y_i) = v_x(x_i, y_i)\mathbf{e}_x + v_y(x_i, y_i)\mathbf{e}_y$ at a position (x_i, y_i) the average velocity components $v_x(x_i, y_i)$ and $v_y(x_i, y_i)$ are calculated by CP-TDE. A set of three time series is measured at three different positions in the $x-y-$plane. The three non-collinear points span a triangle (1, 2, 3) whereas the position (x_i, y_i) corresponds to the geometric barycenter of the triangle [Fig. 2(a), the triangle does not necessarily have to be equilateral]. The only assumption for the

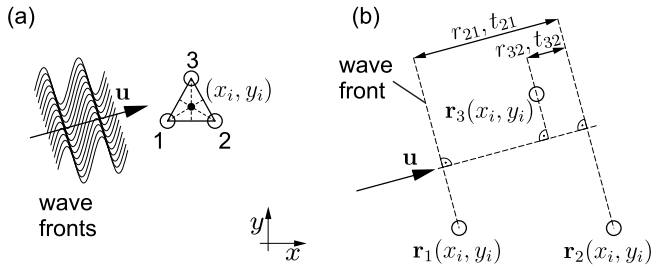

FIG. 2: Illustration of the three points used for 3-point CP-TDE velocimetry. (a) Three points (1,2,3) of locations for simultaneous data acquisition. It does not necessarily need to be an equilateral triangle. The studied structures are assumed to be much larger than the average distance between the points to assume plane wave propagation. (b) Geometry for time lag calculation.

derivation of the velocity field is that the structures keep their shape and velocity vector constant while passing the triangle. The smaller the triangle compared to any structure, the better this assumption is fulfilled (since the time any structure needs to pass decreases with size). In the following we consider structures and wavelengths much larger than the distance between the triangle points and hence we can safely assume that structures passing across the triangle propagate like plane waves, as shown in Fig. 2(b). The wave front with the velocity vector $\mathbf{v}$ passes the array of three points. Based on the incident angle of the velocity vector, the plane wave front is detected at the three points #1, #2 and #3 with time lags $t_{21} = t_2 - t_1$ and $t_{32} = t_3 - t_2$. According to Fig. 2 the distances are given by $s_{21} = \langle \mathbf{v}, \mathbf{r}_{21} \rangle / |\mathbf{v}|$ and $s_{32} = \langle \mathbf{v}, \mathbf{r}_{32} \rangle / |\mathbf{v}|$, with $\mathbf{r}_{21} = \mathbf{r}_2 - \mathbf{r}_1$ and $\mathbf{r}_{32} = \mathbf{r}_3 - \mathbf{r}_2$. Consequently, the time lags are given by

$$t_{21} = \frac{\langle \mathbf{v}, \mathbf{r}_{21} \rangle}{|\mathbf{v}|^2} , \qquad t_{32} = \frac{\langle \mathbf{v}, \mathbf{r}_{32} \rangle}{|\mathbf{v}|^2} . \tag{1}$$

Solving for the components of $\mathbf{v}$ yields

$$v_x = \frac{(r_{21y} r_{32x} - r_{21x} r_{32y})(-r_{32y} t_{21} + r_{21y} t_{32})}{(r_{21x} t_{32} - r_{32x} t_{21})^2 + (r_{21y} t_{32} - r_{32y} t_{21})^2} \tag{2}$$

$$v_y = \frac{(r_{21y} r_{32x} - r_{21x} r_{32y})(r_{32x} t_{21} - r_{21x} t_{32})}{(r_{21x} t_{32} - r_{32x} t_{21})^2 + (r_{21y} t_{32} - r_{32y} t_{21})^2} . \tag{3}$$

The time lags t_{21} and t_{32} are calculated frequency-resolved from the cross-phase spectra $\theta_{21}(f)$ and $\theta_{32}(f)$

according to

$$\Delta t_{kl}(f) \;=\; \frac{\Delta\theta_{kl}(f)}{2\pi f}\;. \tag{4}$$

The cross-phase spectra are calculated from the angle of the cross-power spectral density $\sphericalangle P_{kl}$. The cross-power spectral density (CPSD) is the distribution of cross-power per unit frequency. For the fluctuating quantities $s_k(t)$ and $s_l(t)$ the CPSD is defined as [32]

$$P_{kl}(\omega) = \int_{-\infty}^{\infty} R_{kl}(t)\mathrm{e}^{-\mathrm{i}\omega t}\mathrm{d}t\;, \tag{5}$$

with R_{kl} being the cross-correlation, defined as

$$R_{kl}(t) = \int_{-\infty}^{\infty} s_k^*(\tau)\cdot s_l(\tau+t)\mathrm{d}\tau \tag{6}$$

where s_k^* denotes the complex conjugate of s_k. To obtain a good spatial resolution in all directions, it is a reasonable choice to use the smallest possible triangle, if possible where the edge angles are close to 60°. The size of the triangle, i.e., the distance between the points d, determines the minimum size of the structures for that a velocity can be detected. Here the Nyquist limit gives the smallest detectable structures with $a_{\min} > 2d$.

Figure 3 illustrates the three point pixel array at one specific position as used in the present work in fast camera data. As an example in Fig. 3(a) is shown the camera frame of Fig. 12(e_1) for $B = 160\,\mathrm{mT}$ at $\tau = 0\,\mu\mathrm{s}$. The barycenter of the pixel array (at $x = -1.7\,\mathrm{cm}$ and $y = -1.8\,\mathrm{cm}$) corresponds to a single point where the velocity vector is calculated. The three pixels can be better distinguished in the zoomed plot in Fig. 3(b). The size of the pixel array is considerably smaller than the observed wave structures in the plasma. Thus plane wave propagation across the pixels can be assumed.

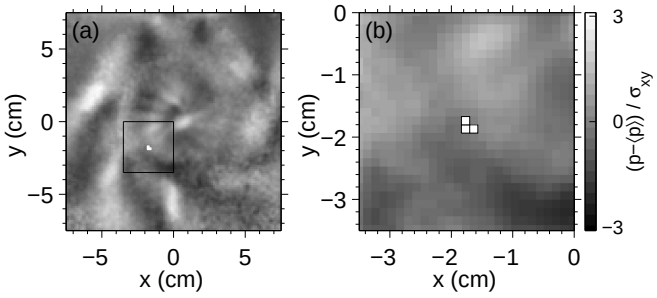

FIG. 3: The pixel array used for 3-point CP-TDE velocimetry. (a) This image is taken from the camera frame shown in Fig. 12(e_1) for $B = 160\,\mathrm{mT}$. The three points are shown as white pixels. Here the velocity vector is calculated at the position $x = -1.7\,\mathrm{cm}$ and $y = -1.8\,\mathrm{cm}$. (b) Zoomed region indicated by the black frame in Fig. (a).

Equations (1) to (3) show, that the velocity vector is calculated from just two time delays (in this example from the pairs 1-2 and 2-3). Since three points give three possible pairs (1-2, 2-3 and 3-1) the number of equations is larger than unknowns and the solution for this system of equations is overdetermined. However, in a real physical system the presence of noise and the fact that the wave fronts can change their shape while passing the three points, especially in turbulent dynamical systems, lead to the fact, that the solution of each possible pair is independent. In this sense the three possible combinations (1-2 and 2-3; 2-3 and 3-1; 3-1 and 1-2) can be used to independently calculate the velocity vector from the same original data from the time series measured at the points #1, #2 and #3. Finally this method gives three realizations of the calculated velocity at the barycenter of the three points from one set of measurements. We have checked rigorously that the velocities calculated are similar, independent which of the pairs are chosen. Averaging over these three realizations gives the best estimate of the velocity at the barycenter of the chosen triangle of points. In Fig. 4 we compare the velocity vector fields calculated from the three different sets of pairs. The

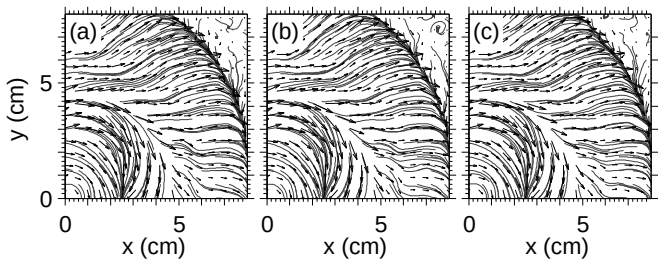

FIG. 4: Velocity vector fields using 3-point CP-TDE velocimetry from the identical measurement for the three realizations of the permutations (a) 1-2 and 2-3, (b) 2-3 and 3-1, (c) 3-1 and 1-2. This example is discussed in details in Fig. 13(d). Superimposed shown are streamline plots calculated for each vector field. The velocity field is measured at $B = 160\,\mathrm{mT}$ and averaged over the strongest frequency component over the frequency range $2.5 - 4.5\,\mathrm{kHz}$. For visibility only every 4th vector in x and y direction is shown.

average variation of the vectors, i.e., its absolute values and the angles, between the three realizations is about $5 - 15\,\%$. In the edge the signal-to-noise ratio is much lower and thus the measured time lags are more influenced by noise. Especially in the center of the plasma averaging over the three realizations is useful to obtain a better estimate of the velocity vectors by reducing the noise. After calculation of the vector components a median filter is applied to exclude local outliers of the vector components.

2.1. Effect of shear on evaluation of radial velocity

It is important to keep in mind that the 3-point CP-TDE velocimetry method calculates the time-averaged

velocity vector of wave fronts. In case the velocity vector of propagating structures is not perpendicular to the wave fronts [see Fig. 5], the wave front vector obtained

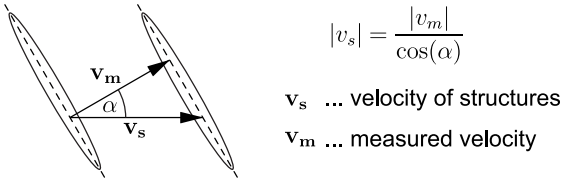

FIG. 5: In case the tilt angle α of propagating structures can be estimated, the velocity of the structures v_s can be calculated from the measured wave front velocity v_m.

from 3-point CP-TDE is not parallel to the velocity vector. However, if an analysis method exists capable to estimate the tilt angle α, the true velocity of the structures v_s can be calculated by $|v_s| = |v_m| \cos(\alpha)$, with v_m being the obtained velocity component from 3-point CP-TDE velocimetry. Figure 6 demonstrates the influence of tilted wave fronts in cylindrical geometry by a calculation of the velocity field using 3-point CP-TDE velocimetry of a modeled azimuthally propagating $m_\phi = 2$ eigenmode [compare Fig. 6(a)], with ϕ being the azimuthal coordinate. Without shear in radial direction the velocity field

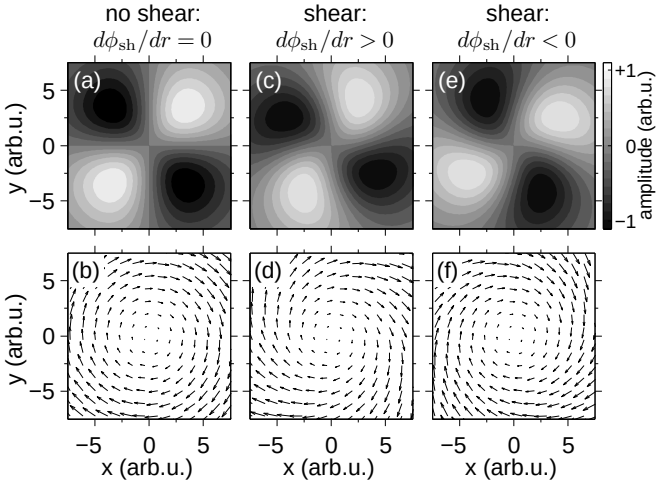

FIG. 6: Dependence of the 3-point CP-TDE velocimetry on sheared structures. The upper row (a,c,e) shows a modeled azimuthal $m_\phi = 2$ eigenmode structure $S(r, \phi_{\rm sh}, t)$ at $t = 0$ propagating in clockwise direction with $S = A(r) \sin(m\omega t + \phi_{\rm sh}(r))$. $A(r)$ is the radial dependent amplitude $A = r\sigma^{-2} \exp\left\{-r^2(\sqrt{2}\sigma)^{-2}\right\}$, $\phi_{\rm sh}(r)$ is the radial dependent shear, $\omega = d\phi/dt$ the angular frequency and $\sigma = 4.3$ the assumed standard deviation of the radial density profile. The lower row (b,d,f) shows the calculated velocity vector fields.

has only azimuthal components [compare Fig. 6(b)]. If a radial shear is present [Figs. 6(c,e)], the velocity field also consists radial velocity components [Fig. 6(d,f)]. The radial velocity components depend on the shear direction and on the azimuthal propagation direction of the structures. For a radial shear $d\phi_{\rm sh}/dr > 0$ an outward radial velocity component arises, and for a radial shear $d\phi_{\rm sh}/dr < 0$ an inward radial velocity component arises. This effect needs to be regarded when interpreting 2D velocity fields [29]. The more turbulent a system is, the less stable are the mode structures [33, 34]. If then the radial shear of the structures randomly change in time, the influence of the shear on the time-averaged velocity field can again be small.

The 3-point CP-TDE velocimtry can also be applied to calculate the time-averaged velocity field of single events such as blobs or eddies. For these structures a reasonable frequency needs to be determined [compare Eq. (4)]. A very simple approach is using $f \approx v/\lambda$, where v is the velocity and λ is the size (or the wavelength) of the structure. The above discussed influence of the shape of these structures is also valid in the same way here.

3. EXPERIMENTAL SETUP

The experimental work has been performed in the Controlled Shear Decorrelation eXperiment (CSDX) [6, 35]. The apparatus consists of a 2.8 m long discharge tube with a radius of 0.1 m. A magnetized argon plasma is produced by helicon discharge using an $m = 1$ antenna (radius 7.5 cm) with typical operating parameters of 1.6 kW rf input power and neutral gas pressure of 0.42 Pa. Finally, since we wanted to study very complex turbulent regimes, we performed these experiments with insulating end boundaries. In previous studies it was shown that the end boundaries are crucial for the system to be driven into broadband turbulence [8, 36].

The azimuthal plasma cross-section is diagnosed by fast imaging. A Phantom V710 high speed camera detects emission from neutral atoms and ions, respectively, with a typical sampling frequency of 210, 526 Hz. To roughly distinguish between emission from neutrals and ions two different optical filters have been used [neutral argon Ar I (longpass filter for wavelength $>$ 650 nm), singly ionized argon Ar II (band pass filter with FWHM from 410 nm to 490 nm)]. For minimizing the contribution of parallel plasma dynamics the parallax and the depth of field ($\sim$ 10 cm) is reduced by using a telescope to image the plasma onto the camera chip. A refractive 1.2 m, $f/8$ Celestron C6-RGT telescope is positioned 7 m away from the focal plane in the plasma (1 m downstream from the source). A more detailed description of the experimental setup is given in Refs. [6, 31]. Temperature fluctuations are neglected and it is assumed light fluctuations represent the dynamics of density fluctuations [21, 30, 31]. The plasma dynamics and the average plasma profile in CSDX in helicon discharge mode vary strongly with ambient magnetic field [6]. The time-averaged density profile peaks in the center and decays within $\approx$ 5 cm towards the edge. With higher magnetic fields the profiles ($n_{\rm e}$ and light intensity) become narrower [37].

4. 2D VELOCITY FIELDS OF HELICON PLASMA REGIMES

In the following 3-point CP-TDE velocimetry is applied to two different plasma regimes. The level of nonlinear coupling and in turn the complexity of dynamics increases with higher magnetic field strengths [6]. The first regime at $B = 90\,\mathrm{mT}$ is dominated by dynamics of quasi-coherent drift waves in the density gradient region. The dynamics of the second regime at $B = 160\,\mathrm{mT}$ is much more complex, i.e., while combined drift wave-Kelvin Helmholtz (KH) activity is present between density gradient and edge, other waves propagating in ion diamagnetic drift direction are present in the center of the plasma.

At magnetic fields below 100 mT the plasma dynamics is dominated by quasi-coherent drift waves in the density gradient region at radii between $2\,\mathrm{cm} < \mathrm{r} < 5\,\mathrm{cm}$. With increasing B-field a considerable shear in $\omega(r)$ evolves in the edge resulting in a combined drift-KH system between density gradient and edge. At magnetic fields between $120\,\mathrm{mT} < \mathrm{B} < 180\,\mathrm{mT}$ high mode numbers with $m_\phi \approx -5$ to $m_\phi \approx -15$ appear in the center of the plasma at radii $r < 2\,\mathrm{cm}$ [6] propagating in the ion diamagnetic drift direction, i.e., the opposite direction to the waves in the combined drift-KH system. Cross-phase analysis of density and potential fluctuations shows that all these instabilities are present simultaneously. Their radial separated regions partially overlap, resulting in intermixed turbulent dynamics [6].

4.1. 3-point CP-TDE velocimetry of drift waves

Previous studies in CSDX have demonstrated a controlled transition to a turbulent state as the magnetic field is increased from 40 mT to 100 mT when the device is configured with insulating boundary conditions [8, 35, 38]. With increasing B, the drift wave fluctuations evolve from narrow-band coherent waves to a state of weak turbulence characterized by broadened frequency and wave number spectra. At $B \sim 90 - 100\,\mathrm{mT}$, the narrow-band coherent eigenmode-like drift wave fluctuations (with a dominant $m_\phi = 3$ mode) coexist with more broadband turbulent fluctuations, in a state of weak turbulence, in the following called quasi-coherent drift waves. Nonlinear energy transfer analyses [39, 40] revealed that the energy is transferred from the higher frequency ($f > 10\,\mathrm{kHz}$, $m_\phi = 3$ mode) turbulent fluctuations to the low frequency ($f < 1\,\mathrm{kHz}$, $m_\phi = 0$ mode) azimuthally symmetric shear flow. The azimuthally symmetric, low frequency sheared flow is driven by the high frequency turbulent plasma fluctuations and thus has the characteristics of a zonal flow. More recent detailed studies for a larger B-field range is given in Ref. [6].

The time-averaged light intensity depicted in Fig. 7(a) peaks in the center at $r = 0\,\mathrm{cm}$ and decays towards the edge within $\approx 5\,\mathrm{cm}$ to 2% of the center peak value.

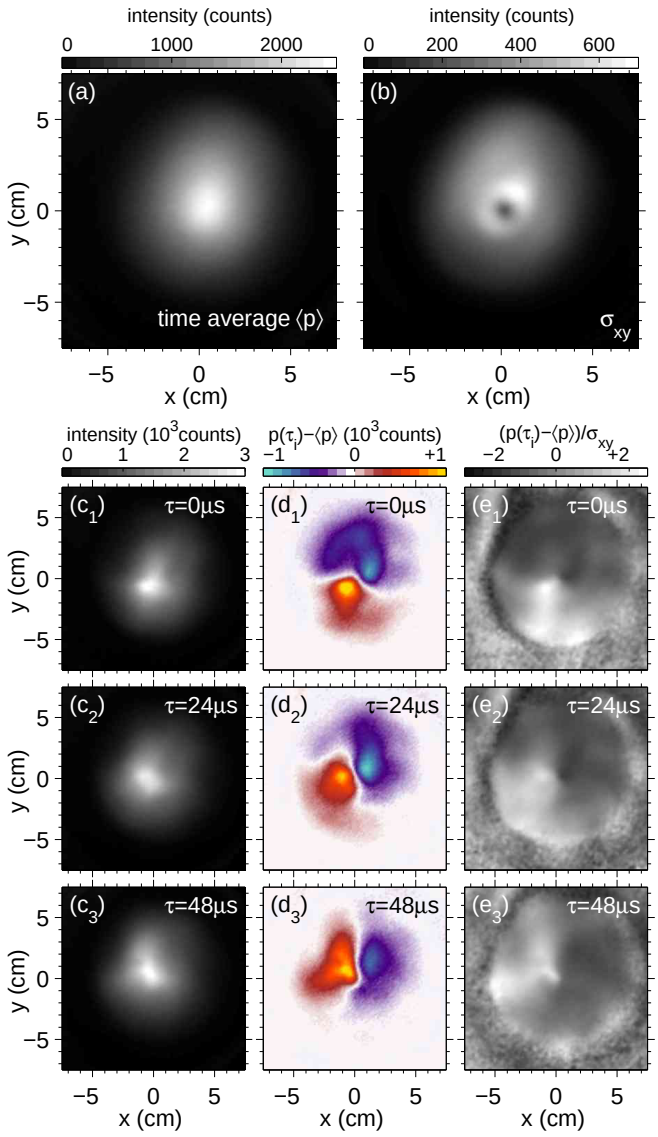

FIG. 7: (Color online) Camera data for the plasma dynamics at $B = 90\,\mathrm{mT}$: (a) time-averaged light intensity (longpass filter $> 650\,\mathrm{nm}$) and (b) standard deviation σ_{xy} for each pixel. In the columns below are image sequences $p(\tau_i)$ of (c) raw images, (d) time average-subtracted raw images and (e) each pixel of each image normalized to its temporal standard deviation to equally emphasize structures in the center (high light intensity) and in the edge (low light intensity).

The standard deviation of light fluctuation is shown in Fig. 7(b). Drift wave fluctuations are the largest in the density gradient between $r = 1 - 5\,\mathrm{cm}$ and in the very center the light fluctuation level is strongly reduced. In the three columns below a sequence of successive camera frames is depicted, illustrating the propagation of wave structures. The first column [Fig. 7(c_{1-3})] shows the raw images and the second column [Fig. 7(d_{1-3})] the light fluctuation by subtracting the time-average [Fig. 7(a)]. A dominant $m_\phi = 1$ mode is propagating clockwise in

the electron diamagnetic drift direction. While propagating, the shape of the mode structure changes, particularly in regions more radially outwards at $r > 2\,\mathrm{cm}$. The third column shows light fluctuations normalized to the standard deviation of each pixel [Fig. 7(e_{1-3})] to emphasize dim structures especially in the edge region. Beyond $r \approx 5\,\mathrm{cm}$ the light fluctuations are close to the noise level. Very weak wave structures are present at $r \sim 5\,\mathrm{cm}$. From light fluctuations the radially resolved frequency spectrum calculated by fast Fourier transform (FFT) and azimuthal averaging is depicted in Fig. 8(a). The largest frequency component is present at 4.9 kHz across the whole radius. The higher harmonics at $2\times, 3\times, 4\times 4.9\,\mathrm{kHz}$ can also be distinguished. Within a broad background, the discrete peaks indicate quasi-coherent wave dynamics dominated by mode structures as seen in Fig. 7(d_{1-3}). For the 3-point CP-TDE velocimetry the light fluctuation data of neighboring camera pixels are used to calculate the cross-power spectra. Figure 8(b) illustrates exemplarily the CPSD [Eq. (5)] between two adjacent pixels. The CPSD peaks at 4.9 kHz and the higher harmonics. The cross-phase $\theta(f)$ is well-defined at frequencies where the CPSD peaks. Figure 8(c) shows the CPSD value at the frequency 4.9 kHz in the azimuthal cross-section. The CPSD spectrum in Fig. 8(b) is measured at the position indicated by the black cross. 3-point CP-TDE velocimetry is applied and the velocities are averaged over the frequency range $3.9 - 5.9\,\mathrm{kHz}$ as this is the frequency range of the dominant mode in the system [see Fig. 8(a)]. The result is shown in Fig. 8(d). The 2D velocity vector field demonstrates wave structures propagating predominantly in azimuthal direction, i.e., in electron diamagnetic direction. Close to the center ($r < 2\,\mathrm{cm}$) the waves are only propagating in just the azimuthal direction. With larger radial position a radial outward velocity component increases leading to an outward spiralling velocity vector field. For this magnetic field configuration the plasma density starts to get very low beyond $r > 5\,\mathrm{cm}$ and the light intensity is too dim to give a definite interpretation of the velocity field.

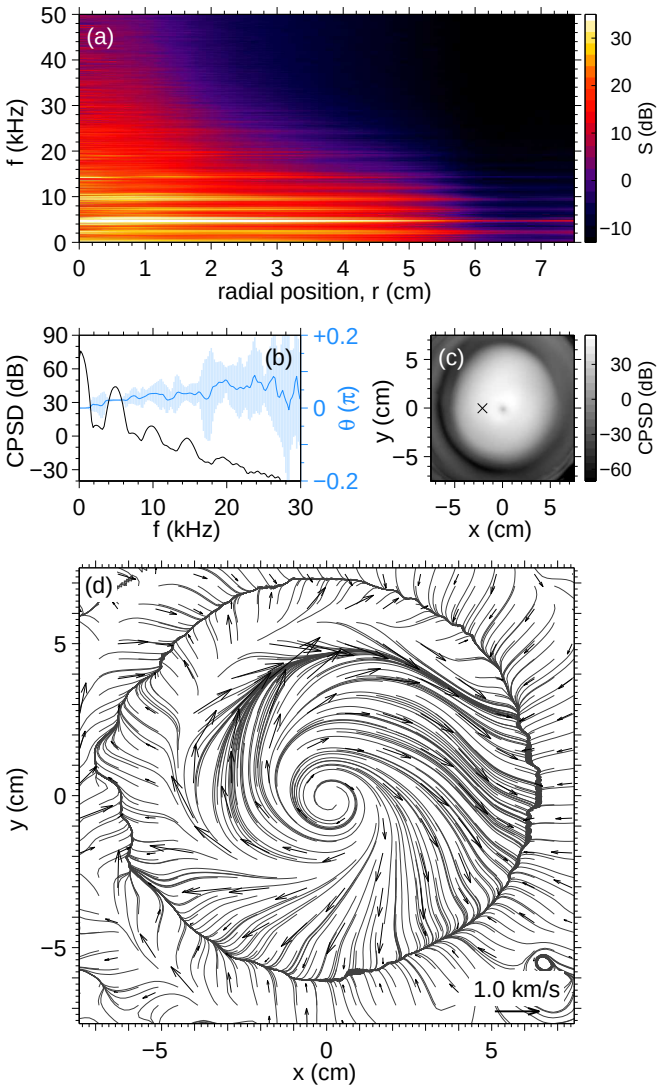

FIG. 8: (Color online) Plasma dynamics at $B = 90\,\mathrm{mT}$ (B-field direction is $\otimes$). (a) From camera data calculated frequency spectra. (b) The cross-power spectral density (CPSD) and the cross-phase of two time series from two adjacent pixels at $r = 1.8\,\mathrm{cm}$ (position of black cross in (c)). (c) The CPSD value at 4.9 kHz in the azimuthal cross-section. (d) Streamline plot and vector field of the calculated velocity field averaged over the frequency range $3.9 - 5.9\,\mathrm{kHz}$. The spatial resolution of the calculation grid is 1.33 mm. For visibility the vector field is averaged over 13.3 mm in each of the directions x and y.

The mode-frequency spectra of the azimuthal eigenmodes are calculated from extracted azimuthal arrays from $\phi = 0$ to 2π and defining the center of $r = 0\,\mathrm{cm}$ at $(x, y) = (0, 0)\,\mathrm{cm}$. Figure 9 shows this spectrum calculated at the radius $r = 2.5\,\mathrm{cm}$. As already visible in the average removed single frames in Fig. 7(d_{1-3}) the dominant mode number is the $m_\phi = +1$ mode propagating in electron diamagnetic direction.

From the 2D velocity vector field the radial profiles of the velocity components in the azimuthal plane, namely the azimuthal velocity v_ϕ and the radial velocity v_r can be calculated. The frequency resolved velocimetry results averaged over the azimuthal coordinate ($\phi = 0$ to 2π) are shown in Fig. 10. The velocity components v_ϕ and v_r are plotted radially resolved and frequency dependent. The ion cyclotron frequency is at $\omega_{ci}/(2\pi) \approx 34.6\,\mathrm{kHz}$. For the whole frequency and radial range the azimuthal propagation is in electron diamagnetic drift direction. In the frequency range up to 20 kHz the radial velocity component v_r is mostly more than two times smaller than the azimuthal velocity, indicating the predominant azimuthal dynamics, as expected for drift wave activity.

An estimation of the temporal fluctuation of the velocity is obtained from time-averaged radial profiles of v_ϕ and v_r at a specific azimuthal angle [Figs. 11(a,b)]. The average and the standard deviation is calculated from

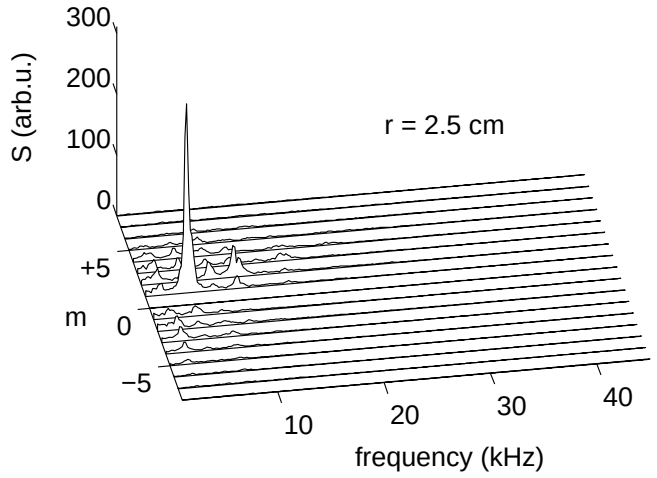

FIG. 9: Mode-frequency spectrum of the plasma dynamics at $B = 90\,\mathrm{mT}$ for the radial position $r = 2.5\,\mathrm{cm}$. The sign of the mode number corresponds to the propagation direction, i.e., positive in electron diamagnetic direction and negative in ion diamagnetic direction.

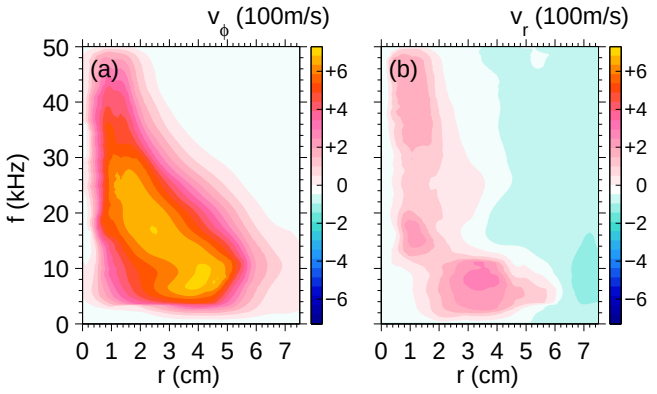

FIG. 10: (Color online) Frequency dependence of azimuthal and radial velocity components for the magnetic field 90 mT: (a) azimuthally averaged azimuthal velocity component v_ϕ and (b) azimuthally averaged radial velocity component v_r.

3-Point CP-TDE velocimetry of five independent time windows of a movie of 5000 frames. According to the $m_\phi = 1$ drift wave mode the velocities are also averaged over the frequency range $3.9 - 5.9\,\mathrm{kHz}$. In this way, if frequency ranges corresponding to specific azimuthal modes are chosen, one can get mode resolved velocity information from these measurements using this method [41]. The temporal deviation of both v_ϕ and v_r is the smallest in the center at $r < 2.5\,\mathrm{cm}$ and gets large in the density gradient $3\,\mathrm{cm} < \mathrm{r} < 5\,\mathrm{cm}$. The deviations would be lower than the statistically error shown here, when the number of realizations is increased. Figure 8(d) indicates that the 2D velocity vector field is not perfectly azimuthally symmetric. From averaging the time-averaged velocity profiles over the full azimuthal circumference $\Delta\phi = 2\pi$, the obtained standard deviation then indicates the variation of the radial profiles due to any azimuthal asymmetry [Fig. 11(c,d)]. The plotted error bars indicate how much the time-averaged profiles vary with the azimuthal angle. For perfect azimuthal symmetry these error bars would be zero. Close to the center the variation is the smallest. For $r > 3\,\mathrm{cm}$ the variation is considerable, especially for the radial velocity component [Fig. 11(d)]. Note that this

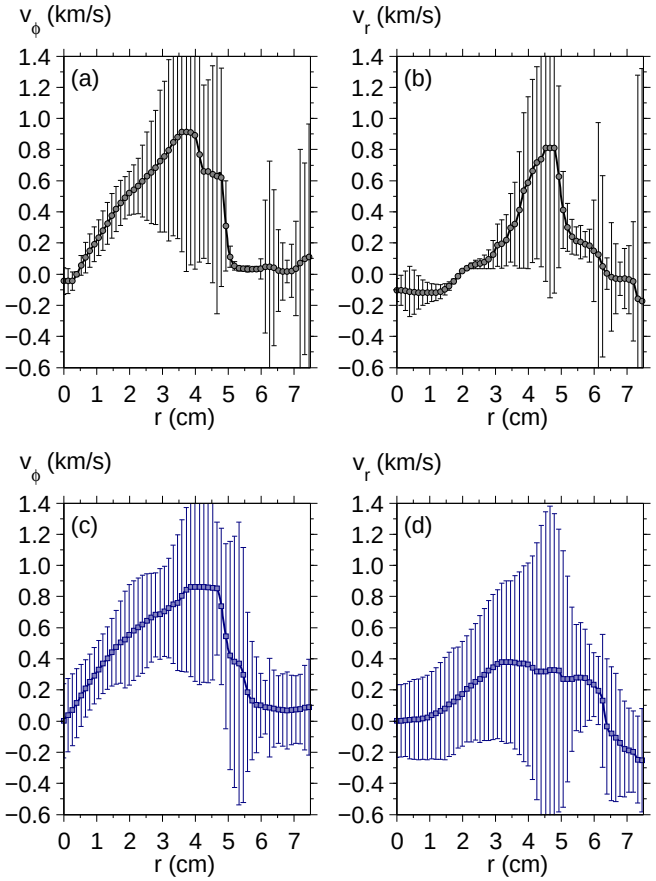

FIG. 11: Radial profiles of (left column) azimuthal velocity v_ϕ and (right column) radial velocity v_r. In (a,b) the values are averaged in time at one azimuthal angle and in (c,d) the profiles are calculated from time-averaged profiles averaged over the full azimuthal circumference $\Delta\phi = 2\pi$. The averaged frequency range is $3.9 - 5.9\,\mathrm{kHz}$. In (a,b) twice the temporal standard deviation is shown as the error intrinsic to this method, in (c,d) once the spatial standard deviation is plotted.

is the region of the largest density and ion pressure gradients that drive the turbulence in CSDX. The corresponding density and electric field fluctuations also contribute to the deviations here. Beyond $r \approx 5\,\mathrm{cm}$, the dynamics is not coherent and the light intensity is low, as can be seen in Fig. 7. The average azimuthal velocity increases approximately linearly between $0\,\mathrm{cm} < \mathrm{r} < 2\,\mathrm{cm}$ from zero to $v_\phi \approx 500\,\mathrm{ms}^{-1}$, whereas the radial velocity component is approximately zero, indicating a nearly pure azimuthal propagation. Between $2\,\mathrm{cm} < \mathrm{r} < 5\,\mathrm{cm}$ the slope of the

azimuthal velocity decreases until it reaches a value of $v_\phi \approx 900\,\mathrm{ms}^{-1}$. Simultaneously a radial outward velocity component increase to $v_r \approx 400\,\mathrm{ms}^{-1}$. However, in this radial region the azimuthal variation becomes large for both velocity components. In the edge region at $r > 5\,\mathrm{cm}$ the wave amplitudes are close to the signal-to-noise level, which especially leads to increased errors. The uncertainties result from the turbulent dynamics of velocity shear driven fluctuations. Here the average azimuthal velocity is close to zero. The average radial velocity varies from zero to $v_r \approx -200\,\mathrm{ms}^{-1}$.

4.2. 3-point CP-TDE velocimetry of coupled instabilities

At 160 mT the plasma dynamics is more complex due to the presence of different wave types at different radial locations. Figures 12(a) and (b) show the time-averaged camera frame and the standard deviation of a movie containing 5000 frames. Compared to Fig. 7(a,b) the light intensity of the plasma peaks more pronounced at smaller radii ($r < 2\,\mathrm{cm}$) and the region of the strongest fluctuation level also shifts more towards the center. This transition has been studied in detail in Refs. [6, 37] and can be explained in the frame of the formation of the blue core in argon plasma helicon mode. The time resolved camera raw images in Fig. 12(c) show the narrow peaked light intensity in the center. Very dim but visible between $0\,\mathrm{cm} < \mathrm{r} < 2\,\mathrm{cm}$ are modes ($|m_\phi| \approx 5$ to $|m_\phi| \approx 15$) with a low amplitude. Particularly these modes propagate in the ion diamagnetic drift direction, i.e., opposite to the drift waves in the gradient region. In Refs. [6, 37] this dynamics have been shown to be well separated from drift wave dynamics in the density gradient region ($2\,\mathrm{cm} < \mathrm{r} < 5\,\mathrm{cm}$). These waves can be better distinguished by subtracting the average [Fig. 12(d)] and normalization to the standard deviation [Fig. 12(e)]. A mode structure of $m_\phi \approx 7$ reaching from $r \approx 3\,\mathrm{cm}$ far into the edge at $r \approx 7\,\mathrm{cm}$ propagates in the electron diamagnetic drift direction (here clockwise) and the higher inner mode structure propagates in the opposite direction (counter-clockwise). The propagation direction of the inner modes is difficult to deduce from the single frames (The spatiotemporal plot in Ref. [6] Fig. 12(e) clearly demonstrates propagation of these core fluctuations in the ion diamagnetic direction). Superimposed to the high modes in the center is a $m_\phi = 2-3$ mode propagating in the electron diamagnetic drift direction [6].

Figure 13(a) shows the frequency spectrogram calculated from the camera data. The strongest frequency components from ($0\,\mathrm{cm} < \mathrm{r} < 5\,\mathrm{cm}$) are located at $\sim 2.5\,\mathrm{kHz}$. In the core region ($0\,\mathrm{cm} < \mathrm{r} < 3\,\mathrm{cm}$) broadband components are present up to 50 kHz. Separated at the edge, frequency components between $1-20\,\mathrm{kHz}$ are present. The study of the cross-phase between density and potential fluctuations in Ref. [6] suggests that these instabilities may be Kelvin-Helmholtz (KH) in the edge and drift waves in the density gradient. The origin of the ion-wave-like mode in the center is still under discussion. Figure 13(b) shows an example of the CPSD and the cross-phase between two time series measured at two adjacent pixels at a radius of $r = 1.8\,\mathrm{cm}$. The cross-phase is well defined at the frequency band between $2.5-4.5\,\mathrm{kHz}$, where also the CPSD peaks. Figure 13(c) shows that the CPSD at 3.5 kHz is well measurable in the azimuthal cross-section. The resulting velocity field averaged over the frequency band $2.5-4.5\,\mathrm{kHz}$ is illustrated

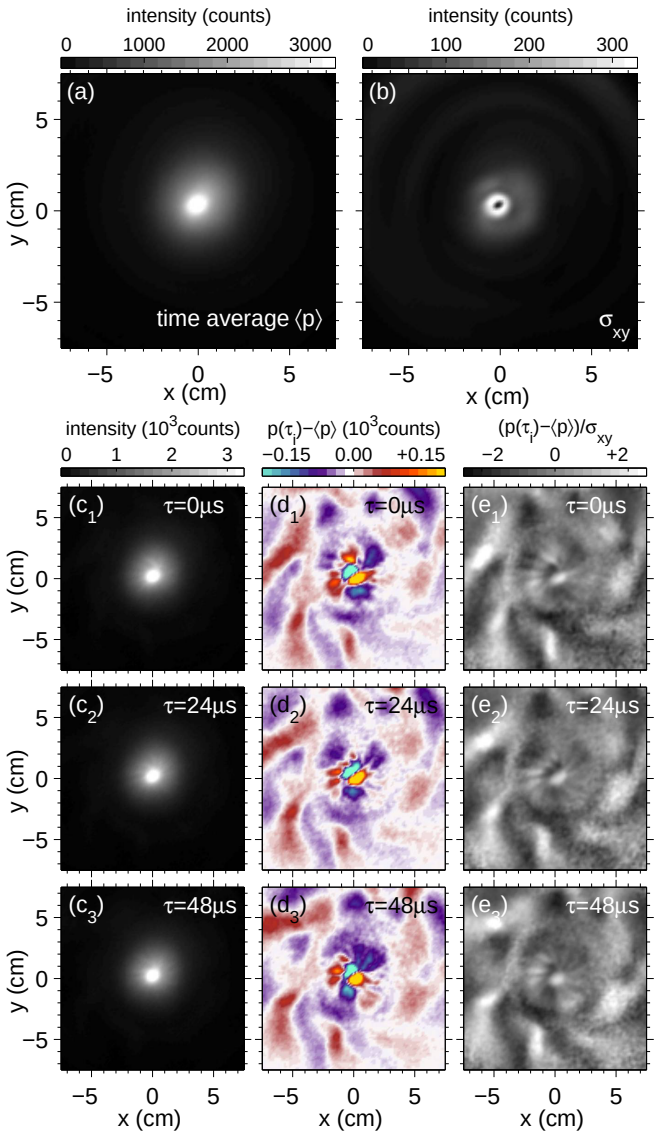

FIG. 12: (Color online) Camera data for the plasma dynamics at $B = 160\,\mathrm{mT}$: (a) time-averaged light intensity (long-pass filter > 650 nm) and (b) standard deviation σ_{xy} for each pixel. In the columns below are image sequences $p(\tau_i)$ of (c) raw images, (d) time average-subtracted raw images and (e) each pixel of each image normalized to its temporal standard deviation to equally emphasize structures in the center (high light intensity) and in the edge (low light intensity).

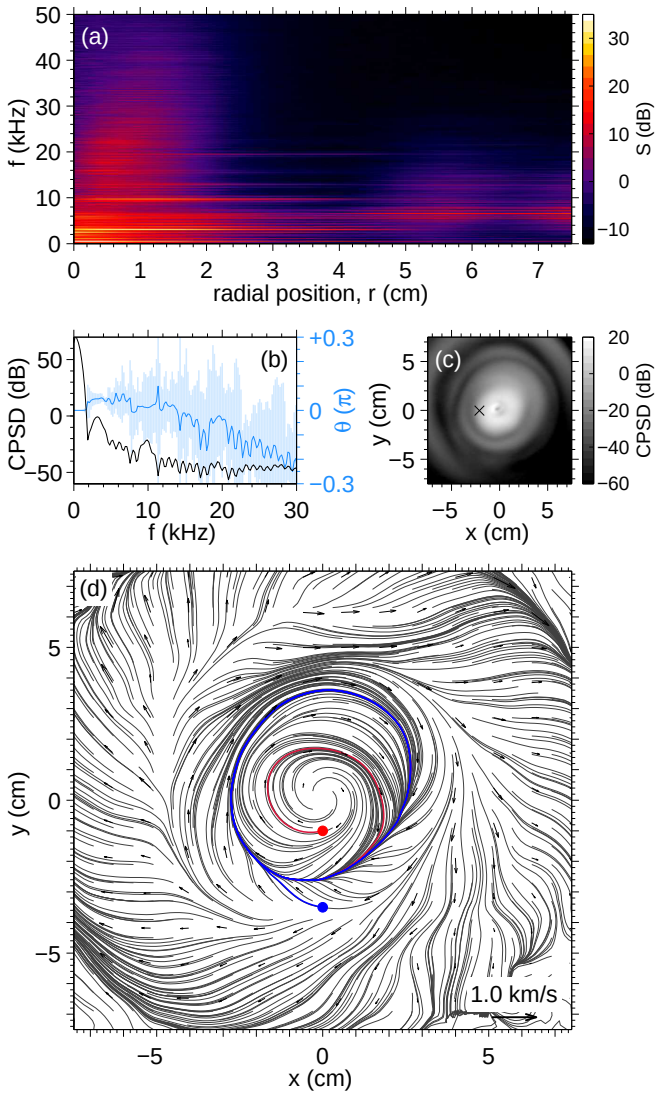

FIG. 13: (Color online) Plasma dynamics at $B = 160\,\mathrm{mT}$. (a) From camera data calculated frequency spectra. (b) The cross-power spectral density (CPSD) and the cross-phase of two time series from two adjacent pixels at $r = 1.8\,\mathrm{cm}$ (position of black cross in (c)). (c) The CPSD value at 3.5 kHz in the azimuthal cross-section. (d) The calculated velocity field averaged over the frequency range $2.5 - 4.5\,\mathrm{kHz}$. The red and blue streamlines demonstrate outward and inward flow, respectively [$x = 0$, red $y = -1.0\,\mathrm{cm}$, blue $y = -3.5\,\mathrm{cm}$]. The spatial resolution of the calculation grid is 1.33 mm. For visibility the vector field is averaged over 13.3 mm in each of the directions x and y.

in Fig. 13(d). The velocity field in the edge is expanded to larger radii when compared to the drift wave case in Fig. 8(d). This can be ascribed to the dynamics in the edge supporting transport of plasma towards the edge resulting in the detection of proper velocity components. Obviously very different dynamics happen between the gradient region and the plasma core. The trajectory emphasized by the red streamline starting in the core at the red solid circle ends on the same path as the trajectory starting more outwards, marked by the blue streamline starting at the blue solid circle. This inward and outward dynamics has also been observed by velocity analysis of flux measurements and have been studied in details in Ref. [42]. According to the discussion in Sec. 2.1 about the influence of the radial shear of the structures, the radial outward component in the radial range $r > 5\,\mathrm{cm}$ probably results from the temporally constant tilt of the structures [compare frames in Fig. 12(d_{1-3})].

The strong frequency dependence of the azimuthal and radial velocity components is illustrated in Fig. 14. In the same way as in Fig. 10 the velocity vectors are averaged over the azimuthal coordinate. At 160 mT the ion cyclotron frequency is at 61.5 kHz. The azimuthal velocity component [Fig. 14(a)] shows one way azimuthal dynamics below 10 kHz in direction of the electron diamagnetic drift. Above 10 kHz the sign of v_ϕ changes for radii $r < 3\,\mathrm{cm}$, i.e., in the core the propagation points in the ion diamagnetic drift direction. The radial velocity component also shows a strong dependence on the frequency. Below $f \approx 2\,\mathrm{kHz}$ the radial velocity is close to zero in the center and in the gradient region. In the edge an outward velocity component exists. Above $f \approx 2\,\mathrm{kHz}$ a radial inward velocity appears below radii $r \approx 4\,\mathrm{cm}$. The change of sign of the radial velocity could be well seen in the 2D velocity vector field in Fig. 13(d) indicated by the colored streamlines. In the core the red streamline starts spiralling outwards, in the gradient region the blue streamline starts spiralling inwards.

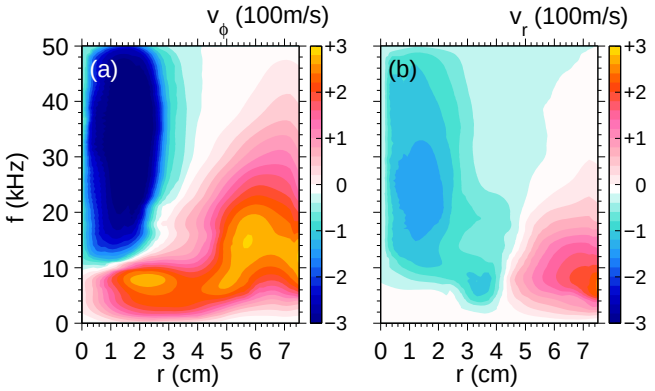

FIG. 14: (Color online) Frequency dependence of azimuthal and radial velocity components for the magnetic field 160 mT: (a) azimuthally averaged azimuthal velocity component v_ϕ and (b) azimuthally averaged radial velocity component v_r.

Figure 15 shows the radial velocity profiles of v_ϕ and v_r averaged over the frequency range $2.5-4.5\,\mathrm{kHz}$ where the largest amplitude in the frequency spectrum is present. Similar to Fig. 11 the Figs. 15(a,b) show the result from averaging over independent realizations in time and Figs. (c,d) the average over the full azimuthal circumference. In time average [Figs. 15(a,b)] the azimuthal velocity increases monotonically from zero the center until $r \approx 4\,\mathrm{cm}$

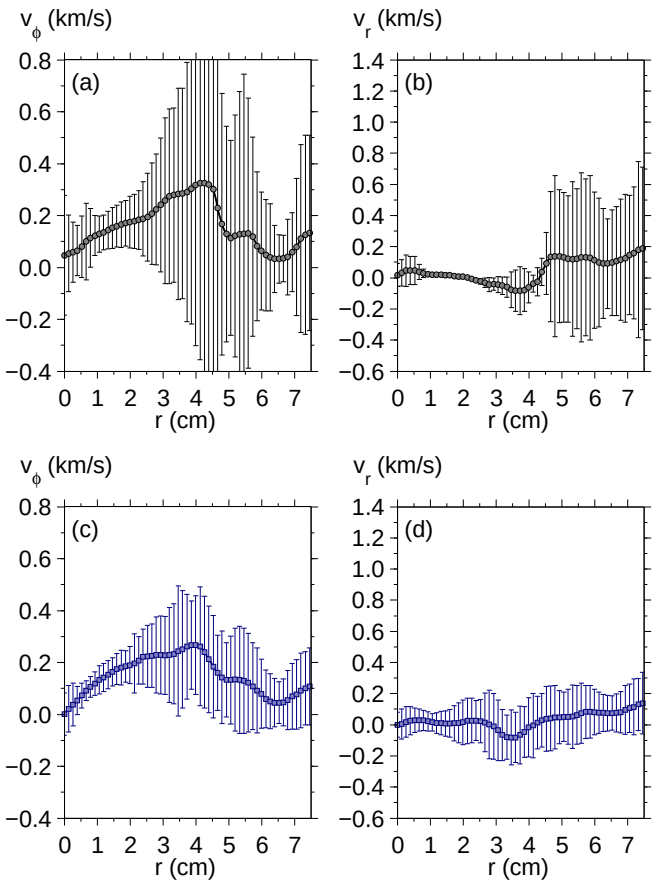

FIG. 15: Radial profiles of (left column) azimuthal velocity v_ϕ and (right column) radial velocity v_r. In (a,b) the values are averaged in time at one azimuthal angle and in (c,d) the profiles are calculated from time-averaged profiles averaged over the full azimuthal circumference $\Delta\phi = 2\pi$. The averaged frequency range is $2.5 - 4.5\,\mathrm{kHz}$. In (a,b) twice the temporal standard deviation is shown as the error intrinsic to this method, in (c,d) once the spatial standard deviation is plotted.

to values about $350\,\mathrm{ms}^{-1}$ and decreases rapidly to zero for $r > 4.5\,\mathrm{cm}$. In the center for $r < 3\,\mathrm{cm}$, the variation of v_ϕ is the smallest. The variation increases to large values in the gradient region indicating turbulence, that leads to considerable fluctuations of the time delays measured by the cross-phases between the time series. For $r < 3\,\mathrm{cm}$ the radial velocity is close to zero. In the radial range $2.5\,\mathrm{cm} < \mathrm{r} < 4.5\,\mathrm{cm}$ the radial velocity points inward with values about $\approx -100\,\mathrm{ms}^{-2}$ until it increases in the edge to positive values of about $\approx +100\,\mathrm{ms}^{-2}$. In the edge the error bars are high as both the turbulence fluctuation level is high [also see [Fig. 13 in Ref. [6]]] and the light intensity drops [see Fig. 12]. More ensemble averaging in time probably might statistically reduce the temporal error calculated. In the azimuthally averaged picture of the time-averaged profiles [Figs. 15(c,d)] a variation is detected indicating azimuthal asymmetry. When compared to the 90 mT case the asymmetry is not as high [compare Fig. 11(c,d)], but still considerable.

Mode-frequency spectra for different radii can help identifying the underlying eigenmode dynamics in the different radial regions. Figure 16 shows mode-frequency spectra at two radii, i.e., within the core at $r = 1.3\,\mathrm{cm}$ and in the gradient region at $r = 2.5\,\mathrm{cm}$. In the core

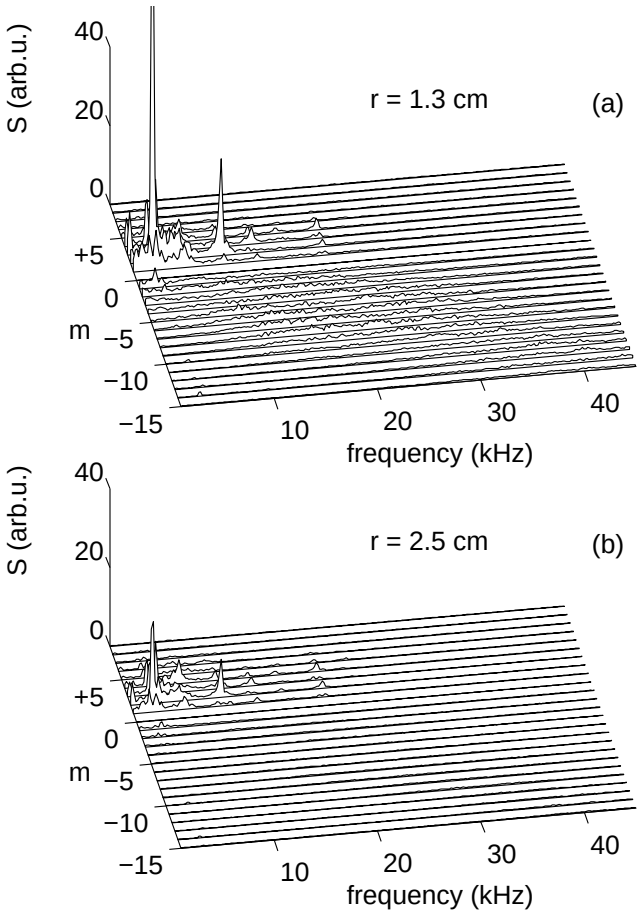

FIG. 16: Mode-frequency spectra of the plasma dynamics at $B = 160\,\mathrm{mT}$ for the radial positions (a) $r = 1.3\,\mathrm{cm}$ and (b) $r = 2.5\,\mathrm{cm}$. The sign of the mode number corresponds to the propagation direction, i.e., positive in electron diamagnetic direction and negative in ion diamagnetic direction.

[Fig. 16(a)] the strongest amplitudes result from drift wave modes $m_\phi = +1$ to $m_\phi = +4$ in the frequency range below $\approx 10\,\mathrm{kHz}$. These modes propagate in electron diamagnetic drift direction. In addition a broad distribution of negative mode numbers between $m_\phi = -1$ to $m_\phi = -15$ is present, which propagate in ion diamagnetic drift direction. Across the frequency range $f \approx 10 - 30\,\mathrm{kHz}$ these modes show a broadband distribution. While the drift wave modes show distinct peaks indicating quasi-coherence, the opposite propagating broadband distributed modes indicate turbulent dynamics. Note, that in the single camera frames the high mode numbers in the core seem to be more coherent, but when studying the movies with more attention, it becomes clear, that the modes are not azimuthal coher-

ent. Frequently the modes change in local azimuthal sectors resulting in the broad mode number spectrum. At outer radii close to the edge, the mode dynamics change [Fig. 16(b)]. Beyond the steep density gradient region at $r \approx 2.5\,\mathrm{cm}$ the drift wave dynamics remains, i.e., only the positive modes $m_\phi = +1$ to $m_\phi = +4$ are present below $f \approx 10\,\mathrm{kHz}$. When comparing the two spectra with the total frequency spectrum [Fig. 13(a)], it becomes clear, that the broadband frequency components with $f > 10\,\mathrm{kHz}$ in the core region result from the opposite propagating mode structures.

The dynamics in the core can be visualized in the velocity vector fields from 3-point CP-TDE velocimetry by extracting the velocity field from selected frequency ranges. In Fig. 17 the velocity fields of drift waves and of the inner mode structure are shown. Figure 17(a)

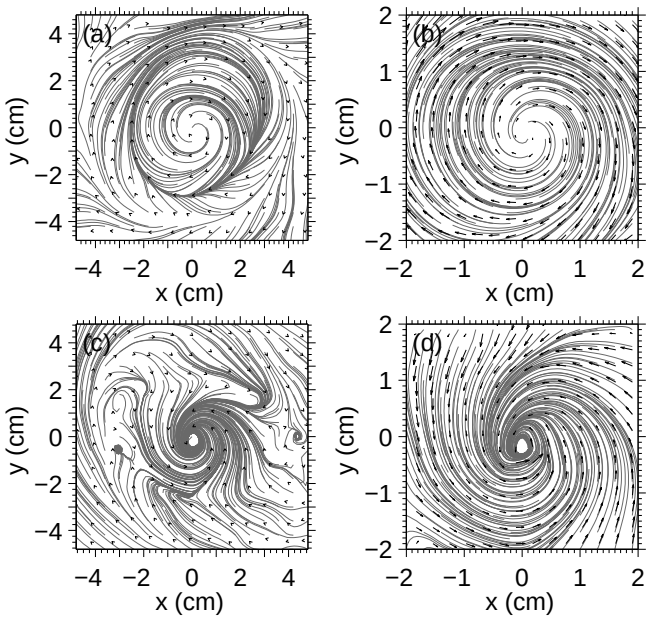

FIG. 17: Velocity vector fields of plasma dynamics at $B = 160\,\mathrm{mT}$ in the frequency ranges of (a,b) $2.5 - 4.5\,\mathrm{kHz}$ and (c,d) $20 - 25\,\mathrm{kHz}$. Both velocity fields are calculated from the same camera dataset. In (a) and (c) the direction is indicated by the arrow heads. The zoomed sections in the right column indicate the details in the plasma core.

shows the velocity field averaged over the dominant frequency peak between $2.5 - 4.5\,\mathrm{kHz}$ [zoomed region of Fig. 13(d)]. Clockwise propagation in electron diamagnetic drift direction is present in the whole azimuthal cross-section. The zoomed plot in Fig. 17(b) demonstrates the one way azimuthal velocity field. Figures 17(c) and (d) show the vector field averaged over the frequency range of $20 - 25\,\mathrm{kHz}$. The streamline plot in Fig. 17(c) indicates the change of sign of v_ϕ at the radius $\approx 4\,\mathrm{cm}$. As visible in Fig. 14 the sign of v_ϕ changes in this frequency range and the structures propagate counter-clockwise in ion diamagnetic drift direction [Fig. 17(d)].

Generally speaking the streamline plots are shown to visualize the 2D vector field. However, their interpretation needs to be done with care, especially thinking about interpreting them as paths for trajectories in such a turbulent system with spatiotemporal fluctuations at multiple scales.

5. DISCUSSION AND CONCLUSIONS

While analyzing the plasma dynamics during the transition to broadband turbulence in CSDX, via different interesting but complex regimes, the knowledge of the velocity components are crucial, but not straightforward. Mach probes were too perturbative in these regimes for CSDX, laser-induced fluorescence spectroscopy was too slow to capture any turbulent dynamics and PIV was not possible at these plasma parameters. Fast framing camera could provide with both the necessary temporal resolution (at $210,526\,\mathrm{frames\ per\ second}$) and with sufficient spatial resolution ($(128 \times 128)\,\mathrm{pixels}$ covering $\approx (17 \times 17)\,\mathrm{cm}$). However, standard traditional two-point TDE did not give reasonable results as explained in details in the introduction. A novel method of using three spatially separated points and using the cross-phase TDE is a simple extension that yielded a lot of important details of the plasma systems studied. Especially for the complex dynamics at $B = 160\,\mathrm{mT}$ where different instabilities are superimposed present simultaneously the 3-point CP-TDE velocimetry demonstrates its capability. Close to the plasma center $m_\phi = 2 - 4$ drift waves are superimposed with modes between $m_\phi = -1$ to $m_\phi \approx -15$ that propagate in opposite direction, i.e., in ion diamagnetic drift direction. The extracted velocity fields show this, when averaged over the correct frequency ranges. Separating the inner mode dynamics from the other dynamics to obtain the velocity field is possible by "filtering" in the frequency ranges. Averaging the velocity over a too large frequency range usually yields in non-meaningful results. In fluids and plasmas not only different frequency and mode components of waves are present at the same time, but also various types of driving instabilities can exist simultaneously. Before the wave velocity can be instability-selectively analyzed, the typical frequency range of the wave type needs to be known. In regions that are dominated by turbulence temporal fluctuation of the velocity components are found to be considerably high. The cylindrical boundary conditions in the present experiment give rise for the dominating azimuthal dynamics. However, the 2D velocity vector fields indicate considerable deviations from perfect azimuthal symmetry.

6. SUMMARY

The 3-point CP-TDE velocimetry is a velocimetry method based on cross-phase time delay estimation. It is introduced to calculate the frequency dependent time-

averaged two-dimensional velocity field of wave dynamics in a plasma (or in a fluid). By assuming plane wave structures and using the data of three time series measured at three positions aligned in a triangle the velocity vectors are calculated. The method has been applied to wave dynamics in a linear magnetized cylindrical plasma. Two different plasma regimes have been investigated. In the first regime the dynamics was dominated by quasi-coherent drift waves. In the calculated 2D velocity field predominantly azimuthal propagation of an $m_\phi = 1$ mode in electron diamagnetic drift direction was seen. Deviations from perfect azimuthal symmetry of the velocity field is observed. The second plasma regime exhibited complex dynamics from multiple driving instabilities. In a combined drift-Kelvin-Helmholtz system between density gradient and edge, propagation in electron diamagnetic drift direction has been observed, and simultaneously weakly developed turbulent mode dynamics of $m_\phi = -1$ to $m_\phi \approx -15$ propagating in the ion diamagnetic direction was present in the plasma core. The velocity fields of these different wave dynamics could be calculated and separated. The advantage using three points for calculating the velocity vectors is, that infinite velocity values are completely avoided. However, interpretation of the 2D vector fields needs to be done with care, especially when structures are tilted, have a blobby character or are small compared to the average distance of the spatial detectors. The 3-point CP-TDE velocimetry is capable to distinguish between dynamics at different time scales and spatial scales, respectively. As soon as high spatiotemporal resolution data is available, this velocimetry method can be supportive especially for rich dynamical regimes exhibiting velocity components entangled in different scales in space and time.

[1] B. B. Kadomtsev, *Plasma Turbulence* (Academic Press, London, New York, 1965).

[2] A. Fujisawa, K. Itoh, H. Iguchi, K. Matsuoka, S. Okamura, A. Shimizu, T. Minami, Y. Yoshimura, K. Nagaoka, C. Takahashi, M. Kojima, H. Nakano, S. Ohsima, S. Nishimura, M. Isobe, C. Suzuki, T. Akiyama, K. Ida, K. Toi, S.-I. Itoh, and P. H. Diamond, Phys. Rev. Lett. **93**, 165002 (2004).

[3] P. H. Diamond, S.-I. Itoh, K. Itoh, and T. S. Hahm, Plasma Phys. Controlled Fusion **47**, R35 (2005).

[4] N. D'Angelo, Phys. Fluids **8**, 1748 (1965).

[5] G. I. Kent, N. C. Jen, and F. F. Chen, Phys. Fluids **12**, 2140 (1969).

[6] S. C. Thakur, C. Brandt, L. Cui, J. J. Gosselin, A. D. Light, and G. R. Tynan, Plasma Sources Sci. Technol. **23**, 044006 (2014).

[7] F. Brochard, E. Gravier, and G. Bonhomme, Phys. Plasmas **12**, 062104 (2005).

[8] S. C. Thakur, M. Xu, P. Manz, N. Fedorczak, C. Holland, and G. R. Tynan, Phys. Plasmas **20**, 012304 (2013).

[9] M. Raffel, C. E. Willert, S. Wereley, and J. Kompenhans, Particle Image Velocimetry (Springer, Berlin, Heidelberg) (1998).

[10] C. Willert and M. Gharib, Exp. Fluids **10**, 181 (1991).

[11] R. Adrian, Exp. Fluids **39**, 159 (2005).

[12] J. A. Leese, C. S. Novak, and B. B. Clark, J. Appl. Meteor. **10**, 118 (1971).

[13] E. Thomas, Phys. Plasmas **6**, 2672 (1999).

[14] T. Miksch and A. Melzer, Phys. Rev. E **75**, 016404 (2007).

[15] J. L. Terry, S. J. Zweben, O. Grulke, M. J. Greenwald, B. LaBombard, J. Nucl. Mater. **337–339**, 322 (2005).

[16] S. J. Zweben, J. L. Terry, B. LaBombard, M. Agostini, M. Greenwald, O. Grulke, J. W. Hughes, D. A. D'Ippolito, S. I. Krasheninnikov, J. R. Myra, D. A. Russell, D. P. Stotler, and M. Umansky, J. Nucl. Mater. **415**, S463 (2011).

[17] I. Cziegler, G. R. Tynan, P. H. Diamond, A. E. Hubbard, J. W. Hughes, J. Irby, and J. L. Terry, Plasma Phys. Controlled Fusion **56**, 075013 (2014).

[18] I. Cziegler, P. H. Diamond, N. Fedorczak, P. Manz, G. R. Tynan, M. Xu, R. M. Churchill, A. E. Hubbard, B. Lipschultz, J. M. Sierchio, J. L. Terry, and C. Theiler, Phys. Plasmas **20**, 055904 (2013).

[19] P. Manz, J. E. Boom, E. Wolfrum, G. Birkenmeier, I. G. J. Classen, N. C. Luhmann Jr., U. Stroth, and the ASDEX Upgrade Team, Plasma Phys. Controlled Fusion **56**, 035010 (2014).

[20] G. R. McKee, R. J. Fonck, D. K. Gupta, D. J. Schlossberg, M. W. Shafer, C. Holland, and G. R. Tynan, Rev. Sci. Instrum. **75**, 3490 (2004).

[21] S. Oldenbürger, C. Brandt, F. Brochard, N. Lemoine and G. Bonhomme, Rev. Sci. Instrum. **81**, 063505 (2010).

[22] T. Munsat and S. J. Zweben, Rev. Sci. Instrum. **77**, 103501 (2006).

[23] M. Jakubowski, R. J. Fonck, C. Fenzi, and G. R. McKee, Rev. Sci. Instrum. **72**, 996 (2001).

[24] D. J. Schlossberg, D. K. Gupta, R. J. Fonck, G. R. McKee, and M. W. Shafer, Rev. Sci. Instrum. **77**, 10F518 (2006).

[25] D. K. Gupta; G. R. McKee, and R. J. Fonck, Rev. Sci. Instrum. **81**, 013501 (2010).

[26] M. Jakubowski, R. J. Fonck, and G. R. McKee, Phys. Rev. Lett. **89**, 265003 (2002).

[27] C. Holland, G. R. Tynan, G. R. McKee, and R. J. Fonck, Rev. Sci. Instrum. **75**, 4278 (2004).

[28] J. H. Yu, C. Holland, G. R. Tynan, G. Y. Antar, and Z. Yan, J. Nucl. Mater. **363–365**, 728 (2007).

[29] N. Fedorczak, P. Manz, S. C. Thakur, M. Xu, G. R. Tynan, G. S. Xu, and S. C. Liu, Phys. Plasmas **19**, 122302 (2012).

[30] G. Y. Antar, J. H. Yu, and G. R. Tynan, Phys. Plasmas **14**, 022301 (2007).

[31] A. D. Light, S. C. Thakur, C. Brandt, Y. Sechrest, G. R. Tynan and T. Munsat, Phys. Plasmas **20**, 082120 (2013).

[32] A. Papoulis, *The Fourier Integral and its Applications* (McGraw-Hill Book Company, 1962).

[33] C. Brandt, O. Grulke, T. Klinger, J. Negrete Jr., G. Bousselin, F. Brochard, G. Bonhomme, and S. Oldenbürger, Phys. Rev. E **84**, 056405 (2011).

[34] C. Brandt, S. C. Thakur, A. D. Light, J. Negrete Jr., and G. R. Tynan, Phys. Rev. Lett. **113**, 265001 (2014).

[35] M. J. Burin, G. R. Tynan, G. Y. Antar, N. A. Crocker and C. Holland, Phys. Plasmas **12**, 052320 (2005).
[36] D. A. D'Ippolito, D. A. Russell, J. R. Myra, S. C. Thakur, G. R. Tynan, and C. Holland, Phys. Plasmas **19**, 102301 (2012).
[37] S. C. Thakur, C. Brandt, L. Cui, J. J. Gosselin, and G. R. Tynan, IEEE Transactions on Plasma Science **43**, 2754 (2015).
[38] G. R. Tynan, C. Holland, J. H. Yu, A. James, D. Nishijima, M. Shimada, and N. Taheri, Plasma Phys. Controlled Fusion **48**, S51 (2006).
[39] M. Xu, G. R. Tynan, C. Holland, Z. Yan, S. H. Müller, and J. H. Yu, Phys. Plasmas **17**, 032311 (2010).
[40] P. Manz, M. Xu, S. C. Thakur, and G. R. Tynan, Plasma Phys. Controlled Fusion **53**, 095001 (2011).
[41] S. C. Thakur, D. McCarren, T. Lee, N. Fedorczak, P. Manz, E. E. Scime, G. R. Tynan, M. Xu, and J. H. Yu, Rev. Sci. Instrum. **83**, 10D708 (2012).
[42] L. Cui, G. R. Tynan, P. H. Diamond, S. C. Thakur, and C. Brandt, Phys. Plasmas **22**, 050704 (2015).